Monthly Notices
of the
ROYAL ASTRONOMICAL SOCIETY

MNRAS **468,** 2506–2516 (2017)
Advance Access publication 2017 March 15

doi:10.1093/mnras/stx640

Is there a giant Kelvin–Helmholtz instability in the sloshing cold front of the Perseus cluster?

S. A. Walker,[1]★ J. Hlavacek-Larrondo,[2] M. Gendron-Marsolais,[2] A. C. Fabian,[3] H. Intema,[4] J. S. Sanders,[5] J. T. Bamford[6] and R. van Weeren[7]

[1]*Astrophysics Science Division, X-ray Astrophysics Laboratory, Code 662, NASA Goddard Space Flight Center, Greenbelt, MD 20771, USA*
[2]*Departement de Physique, Universite de Montreal, Montreal, QC H3C 3J7, Canada*
[3]*Institute of Astronomy, Madingley Road, Cambridge CB3 0HA, UK*
[4]*Leiden Observatory, Leiden University, Niels Bohrweg 2, NL-2333 CA Leiden, the Netherlands*
[5]*Max-Planck-Institute fur extraterrestrische Physik, D-85748 Garching, Germany*
[6]*Department of Applied Mathematics, The University of Leeds, Leeds LS2 9JT, UK*
[7]*Harvard–Smithsonian Center for Astrophysics, 60 Garden Street, Cambridge, MA 02138, USA*

Accepted 2017 March 13. Received 2017 February 15; in original form 2016 December 12

ABSTRACT

Deep observations of nearby galaxy clusters with *Chandra* have revealed concave 'bay' structures in a number of systems (Perseus, Centaurus and Abell 1795), which have similar X-ray and radio properties. These bays have all the properties of cold fronts, where the temperature rises and density falls sharply, but are concave rather than convex. By comparing to simulations of gas sloshing, we find that the bay in the Perseus cluster bears a striking resemblance in its size, location and thermal structure, to a giant (≈50 kpc) roll resulting from Kelvin–Helmholtz instabilities. If true, the morphology of this structure can be compared to simulations to put constraints on the initial average ratio of the thermal and magnetic pressure, $\beta = p_{\rm th}/p_{\rm B}$, throughout the overall cluster before the sloshing occurs, for which we find $\beta = 200$ to best match the observations. Simulations with a stronger magnetic field ($\beta = 100$) are disfavoured, as in these the large Kelvin–Helmholtz rolls do not form, while in simulations with a lower magnetic field ($\beta = 500$), the level of instabilities is much larger than is observed. We find that the bay structures in Centaurus and Abell 1795 may also be explained by such features of gas sloshing.

Key words: galaxies: clusters: intracluster medium – intergalactic medium – X-rays: galaxies: clusters.

1 INTRODUCTION

Chandra observations of the cores of nearby relaxed galaxy clusters have revealed a panoply of structures in the intracluster medium (ICM). Active galactic nuclei (AGN) are seen to inflate bubbles that expand and rise outwards (Fabian et al. 2000; McNamara et al. 2000; Fabian 2012). Minor mergers are seen to induce gas sloshing of the cool core, resulting in spiral patterns of sharp cold fronts, interfaces where the temperature and density jumps dramatically on scales much smaller than the mean free path (Markevitch et al. 2000; Markevitch & Vikhlinin 2007). The resulting imprints of these processes in the ICM provide powerful tools for unravelling both the physics of the ICM itself, and the AGN feedback believed to be responsible for preventing runaway cooling.

In at least three nearby relaxed clusters (Perseus, Centaurus and A1795), these structures include unusual concave 'bay'-like features, which are not easily explained by either AGN feedback or gas sloshing (see Fabian et al. 2006; Walker, Fabian & Kosec 2014; Sanders et al. 2016b), and these are marked by the white arrows in Fig. 1.

These sharp surface brightness discontinuities have all the properties of cold fronts, namely a temperature increase from the more dense side to the less dense side, and widths that are of the same order as the Coulomb mean free path. However, they have a concave curvature, which contrasts with the standard convex curvature of sloshing cold fronts, which has led such features to be also interpreted as the inner rims of cavities. Here, we investigate the possible formation scenarios for these 'bays', comparing their properties in different clusters using a multiwavelength approach of deep *Chandra* and radio observations, together with simulations of gas sloshing (ZuHone & Kowalik 2016) and cavities.

Whilst appearing similar in X-ray images, the inner rims of AGN-inflated bubbles should have different radio properties to inverted cold fronts. Radio mini-haloes in clusters tend to be confined behind cold fronts, with a sharp drop in radio emission across the cold front

★ E-mail: stephen.a.walker@nasa.gov

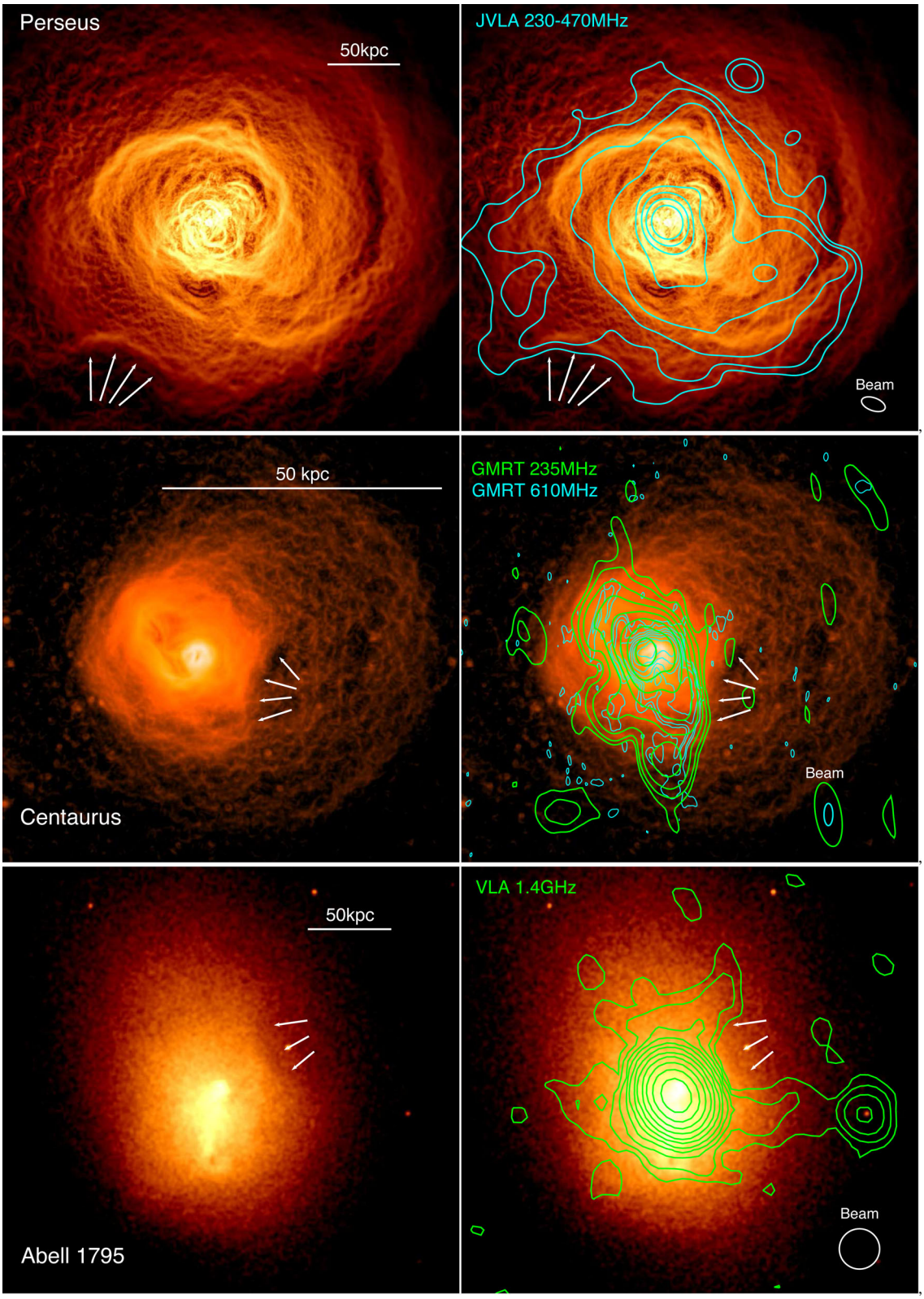

Figure 1. Comparing the bays in the Perseus cluster (top), Centaurus (middle) and A1795 (bottom). Radio contours are overplotted on the X-ray data in the right-hand panels. The radio emission is constrained behind the bays, which themselves contain no radio emission, the opposite to what would be expected for bubbles inflated by AGN feedback. For Perseus and Centaurus, we have filtered the images with the GGM filter to emphasize gradient structure.

edge (Mazzotta & Giacintucci 2008). AGN-inflated bubbles on the other hand should be filled with radio emitting relativistic plasma. A multiwavelength approach will therefore allow us to break this degeneracy.

Simulations of gas sloshing in relaxed clusters predict that as cold fronts rise outwards and age, Kelvin–Helmholtz instabilities (KHIs), brought about by the velocity shear between the cool sloshing core and the outer, hotter cluster ICM can form (e.g. ZuHone, Markevitch & Lee 2011; Roediger et al. 2012, 2013). In simulations, these can grow to sizes of the order of tens of kpc for old cold fronts. These Kelvin–Helmholtz (KH) rolls can produce inverted cold fronts, which are concave, similar to the 'bays' we observe.

In simulations, the development of KHI rolls is very sensitive to the strength of the magnetic field and the level of viscosity, with vastly different structures forming depending on the input values for these. Differences in the cluster microphysics can therefore affect the cold front morphology on scales of tens of kpc (for a review, see Zuhone & Roediger 2016). Because of this, observing large KHIs in real clusters would provide powerful constraints on the magnetic field strength and viscosity in the cluster ICM.

In Section 2, the X-ray and radio data used are discussed. Section 3 compares the properties of the bays in the Perseus, Centaurus and Abell 1795. In Sections 4 and 5, we compare our observations to simulations of cavities and gas sloshing, respectively. In Section 6, we present our conclusions. We use a standard ΛCDM cosmology with $H_0 = 70$ km s^{-1} Mpc^{-1}, $\Omega_{\rm M} = 0.3$ and $\Omega_\Lambda = 0.7$. All errors unless otherwise stated are at the 1σ level.

In this work, the term 'bay' refers to the concave surface brightness discontinuity itself, which, in the analogy with an ocean bay, more accurately corresponds to the 'shoreline' between the water and the land. We refer to the side of the bay towards the cluster centre as 'behind' the bay, while the opposite side is 'in front' of the bay.

2 DATA

2.1 X-ray data

We use deep *Chandra* observations of Perseus (900 ks of ACIS-S data, plus 500 ks of ACIS-I wide field observations), Abell 1795 (710 ks of ACIS-S and ACIS-I) and the Centaurus cluster (760 ks of ACIS-S), tabulated in Table A1 in Appendix A. The data used, and the reduction process, are described in Fabian et al. (2006) and Fabian et al. (2011) for Perseus, in Walker et al. (2014) for Abell 1795, and in Sanders et al. (2016b) and Walker, Sanders & Fabian (2015) for Centaurus.

In short, the *Chandra* data were reduced using the latest version of CIAO (4.8). The events were reprocessed using CHANDRA_REPRO. Light curves were then extracted for each observation, and periods of flaring were removed. Stacked images in the broad 0.7–7.0 keV band were created by first running the script REPROJECT_OBS to reproject the events files, and then FLUX_OBS was used to extract images and produce their exposure maps. For each cluster, the observations were stacked, weighting by the exposure map.

Spectra were extracted using DMEXTRACT, with ARFs and RMFs created using MKWARF and MKACISRMF. The script ACIS_BKGRND_LOOKUP was used to find appropriate blank sky background fields for each observation, which were rescaled so that their count rates in the hard 10–12 keV band matched the observations.

2.2 Radio data

We use deep Karl G. Jansky Very Large Array (JVLA) observations of Perseus (contours shown in the top-right panel of Fig. 1), consisting of 5 h in the B configuration (maximum antenna separation of 11.1 km, synthesized beamwidth of 18.5 arcsec) in the *P* band (230–470 MHz) obtained from a shared-risk proposal. The JVLA is outfitted with new broad-band low-frequency receivers with wider bandwidth. The data reduction was performed with CASA (Common Astronomy Software Applications). A pipeline has been specifically developed to reduce this data set and is presented in detail in Gendron-Marsolais et al. (2017).

The main steps of data reduction can be summarized as follows. The RFI were identified both manually and automatically. The calibration of the data set was conducted after the removal of most of the RFI, and each calibration table was visually inspected, the outliers solutions were identified and removed. Parameters of the clean task were carefully adjusted to take account of the complexity of the structures of Perseus core emission and its high dynamic range. We used a multiscale and multifrequency synthesis-imaging algorithm, a number of Taylor coefficients greater than one, W-projection corrections, a multiscale cleaning algorithm and a cleaning mask limiting regions where emission was expected. A self-calibration was also performed, using gain amplitudes and phase corrections from data to refine the calibration. The resulting image has an rms noise of 0.38 mJy beam^{-1}, a beam size of 22.0 $\times$ 11.4 arcsec and a maximum of 10.58 Jy beam^{-1}.

The Giant Metrewave Radio Telescope (GMRT; Swarup 1991) was used to observe the centre of the Centaurus cluster (NGC 4696) during two 5-h observe sessions in 2012 March (project 21_006; PI Hlavacek-Larrondo). These contours are shown in the middle-right panel of Fig. 1. Data were recorded simultaneously in single-polarization mode at 235 and 610 MHz over 16- and 32-MHz bandwidths, respectively, using 0.13-MHz frequency channel resolution and 16.1-s time resolution. The flux calibrator 3C 286 was observed for 10–15 min at the start and end of both observe sessions. In between, the target field (NGC 4696) was observed in scans of 30 min, interleaved with phase calibrator scans of 5 min. The total time on target is close to 7 h.

The observational data at both frequencies were processed using the SPAM pipeline (Intema 2014) in its default mode. We started by processing of the 235-MHz data using a skymodel for calibration purposes derived from the GMRT 150-MHz sky survey (TGSS ADR1; Intema et al. 2017). The resulting 235-MHz image has a central image sensitivity of 0.95 mJy beam^{-1} and a resolution of 27.7 arcsec $\times$ 11.0 arcsec (PA 10 deg). We used the PYBDSM source extractor (Mohan & Rafferty 2015) to obtain a source model of the image, which we used as a calibration skymodel for processing of the 610-MHz data. The resulting 610-MHz image has a central image sensitivity of 85 μJy beam^{-1} and a resolution of 9.5 arcsec $\times$ 3.8 arcsec (PA 0 deg). In both images, the bright central radio source is surrounded by some image background artefacts due to dynamic range limitations that are known to exist for GMRT observations, increasing the local background rms by a factor of 2–3. However, the artefacts have little effect on the observed radio emission presented in this study.

The 1.4-GHz VLA contours for Abell 1795 shown in the bottom panel of Fig. 1 are taken from Giacintucci et al. (2014).

3 BAY PROPERTIES

Fig. 1 shows Gaussian gradient magnitude (GGM) filtered broad-band (0.7–7.0 keV) *Chandra* X-ray images of Perseus (top) and Centaurus (middle). The GGM filter enhances surface brightness edges in these images (Sanders et al. 2016a; Walker, Sanders & Fabian 2016), increasing the contrast of the edges by around a

factor of 10 for Perseus and Centaurus. Due to the higher redshift and smaller angular size of A1795 (which is at $z = 0.062$, compared to $z = 0.01$ for Centaurus and $z = 0.018$ for Perseus), the normal broad-band *Chandra* image is shown. An unfiltered version of the Perseus *Chandra* image is shown in the top-left panel of Fig. 7, while an unfiltered version of the Centaurus image is shown in fig. 1 of Sanders et al. (2016b). The bays in each cluster are clear and marked with the white arrows. In the right-hand column, we show the radio contours overlain on the X-ray data.

3.1 Widths of the edges

To determine the widths of the bays edges, we fit their surface brightness profiles with a broken power-law model, which is convolved with a Gaussian, as in Sanders et al. (2016a) and Walker et al. (2016). In all three cases, we obtain widths consistent with the known cold fronts in these clusters. For Perseus the upper limit on the width is two times the Coulomb mean free path, while in Centaurus the width of 2 kpc is consistent with the range of widths (0–4 kpc) found for the main cold front in Sanders et al. (2016a). In Abell 1795, the width is consistent with that of the main cold front to the south studied by Markevitch, Vikhlinin & Mazzotta (2001) and Ehlert et al. (2015). This all indicates that transport processes are heavily suppressed across these edges to the same extent as the known cold fronts.

3.2 Temperature, density and metallicity profiles

In Figs 2 and 3, we show projected temperature, metallicity and surface brightness profiles across the edges of the bays in the three clusters. The regions used for extracting these spectra are shown in Fig. A1 in Appendix A. In each case, we see an abrupt temperature jump across the bay, consistent with cold front behaviour. In Perseus and A1795, we also see a significant decline in the metal abundance, from ∼0.5 to ∼0.3 $Z_{\odot}$, which is again consistent with cold front behaviour, where the metal-enriched cluster core is sloshing, leading to sharp falls in metallicity across cold fronts (Roediger et al. 2011). This metallicity structure is also at odds with an AGN-inflated bubble origin for the bays, as typically the bubbles along the jet direction are found to coincide with a metal enhancement (Kirkpatrick, McNamara & Cavagnolo 2011), as they uplift metal-enriched gas from the cluster core. When we continue the profiles further outwards from the cluster core, we see no increase in the metal abundance in front of the bay (i.e. no metal excess in what would be the middle of the cavity). When we compare the metal abundance profile across the bay with that across the 'normal' parts of the cold front next to the bay (which have a convex curvature) in the middle panels of Figs 2 and 3 for Perseus and Abell 1795, respectively (magenta points), we see that the two profiles are consistent with each other.

3.3 Radio properties

All three clusters have radio mini-haloes in their cores. These radio mini-haloes are relatively rare and are confined to the central cooling region of the clusters. Their origin remains a subject of continued debate. There are two leading theories for the radio emission: one is that gas sloshing induced turbulence re-accelerates relativistic electrons in cluster cores (originating from AGN feedback; Gitti, Brunetti & Setti 2002; Gitti et al. 2004), the second is that relativistic cosmic ray protons inelastically collide with thermal protons, generating secondary particles (Pfrommer & Enßlin 2004; Keshet 2010; Keshet & Loeb 2010). Their spatial extent is typically bound by cold fronts (Mazzotta & Giacintucci 2008), believed to be the result of the draped magnetic fields around cold fronts preventing the relativistic electrons from passing through them, constraining them to the inside of the cold front (see the simulation work of ZuHone et al. 2013). In Perseus, we see that the mini-halo is constrained behind the prominent cold front to the west, while in Centaurus and A1795 the mini-haloes are confined behind the cold fronts to the east and south, respectively.

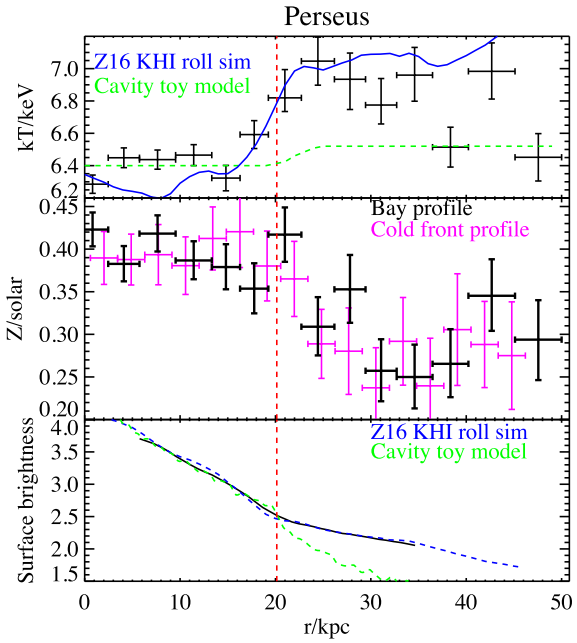

Figure 2. Temperature (top), metallicity (middle) and surface brightness (bottom) profiles over the bay in Perseus. The location of the surface brightness edge is shown by the dashed red line. The temperature jump is clear. The fractional increase in temperature resembles that seen across the bay-shaped KH roll in the simulations of ZuHone & Kowalik (2016, Z16, blue line) shown later in Fig. 7, and is much larger than the temperature jump expected across an empty cavity in our cavity toy model (dashed green line). The metallicity also seems to sharply decrease across the edge (black points), in the same manner as the metal abundance drop over the 'normal' part of the cold front next to the bay (magenta points). In the bottom panel, we compare the projected surface brightness profile across the bay (black) with that across the simulated KH roll (blue dashed) and a toy model of an empty spherical cavity in Perseus (dashed green). The simulated KH roll profile agrees well with the magnitude of the observed surface brightness drop, while the cavity toy model predicts a much bigger surface brightness drop than is observed. As discussed in Section 4, an ellipsoidal cavity toy model was also tested, but this increases the surface brightness profile discrepancy.

Interestingly, we see that in all three clusters, the radio haloes are also constrained behind the bays, adding support to the idea that these bays are cold fronts that are concave rather than convex. Previously for Perseus, Fabian et al. (2011) compared the X-ray image to early 49-cm VLA data from Sijbring (1993) and reported that the bay is coincident with a minimum in radio flux. This radio behaviour is the opposite to what would be expected from a bubble inflated through AGN feedback, which are typically found to be filled with radio emitting relativistic plasma. For each cluster, the radio level in front of the bays is consistent with the background level. The typical radio flux expected if these were cavities is at least the same order as that of the radio halo, and would be easily seen if present.

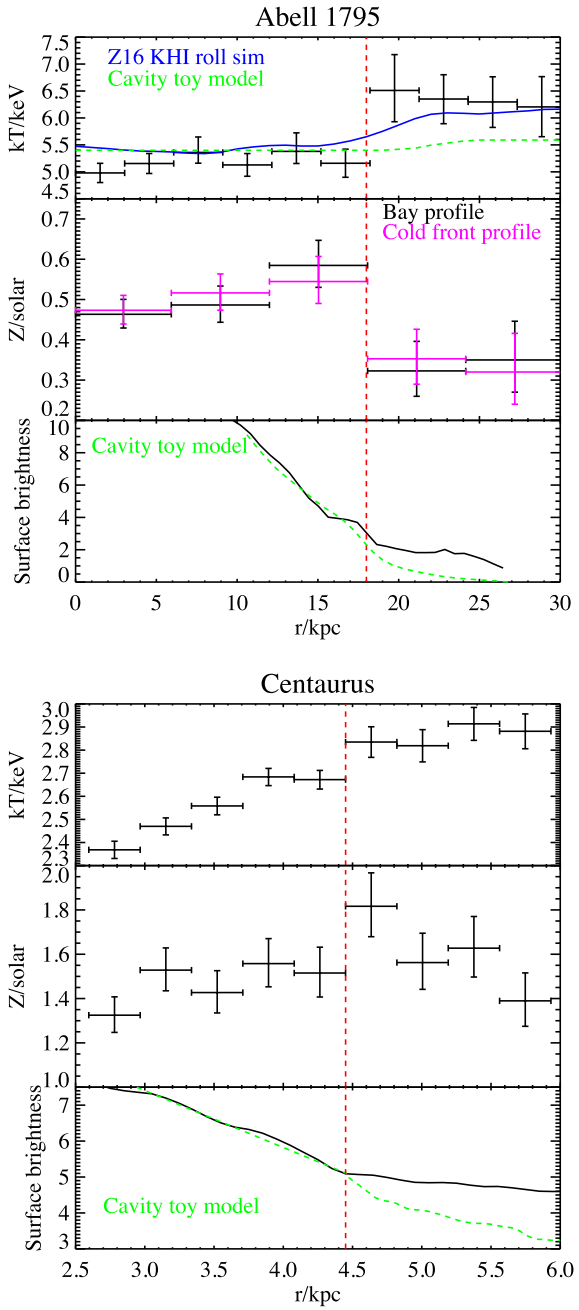

Figure 3. Same as Fig. 2 but for the bays in Abell 1795 (top) and the Centaurus cluster (bottom). As with the Perseus bay, we see that for Abell 1795 the temperature jump is roughly consistent with that across a simulated KHI roll, and is much larger than the jump predicted by our empty cavity toy model. The cavity toy model again overestimates the surface brightness drop.

3.4 Geometry

One immediately obvious characteristic of the bays is that they are only present on one side of the cluster. Typically, for AGN-inflated cavities, one would expect there to be a second cavity on the opposite side of the cluster resulting from the other jet direction.

The locations of the bays in Perseus and Abell 1795 relative to their main outer cold front are similar, both lying around 130 deg clockwise or counterclockwise from the main cold front. This is shown in Fig. 4, in which we have reflected and rotated the image

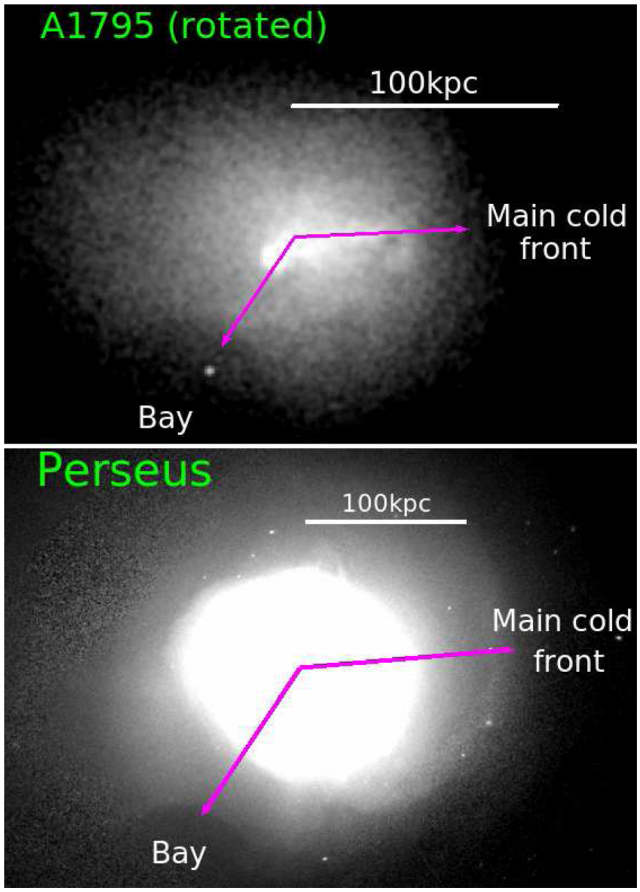

Figure 4. Here, we have flipped and rotated the image of Abell 1795 to compare to Perseus. The separation angle between the main cold front and the bay in each system is similar at around 130 deg.

of Abell 1795 to compare to Perseus. This similarity suggests at a link between the location of the main cold front and the bays in these systems. However, the spatial scale of these features in Abell 1795 is roughly half that of the same features in Perseus, despite both clusters having roughly the same total mass of 7.0×10^{14} $M_{\odot}$ (Bautz et al. 2009; Simionescu et al. 2011).

The bay in Centaurus differs from those in Perseus and Abell 1795, as it is much closer to the cluster core (around 20 kpc from the core compared to 100 kpc in Perseus). In Centaurus, there is no significant evidence for a metallicity jump across the bay. There is a high metallicity point immediately in front of the bay, though the significance of this is low. The temperature jump is much less pronounced (a 7 per cent jump from 2.7 to 2.9 keV, compared to the ∼20 per cent jump seen in Perseus and A1795). This may be because the bay in Centaurus is much closer to the cluster core, where metals are being deposited into the ICM from the BCG, and where the effect of AGN is greater. Centaurus is well known to have an extremely high central metal abundance reaching up to 2.5 $Z_{\odot}$ (Fabian et al. 2005), suggesting that the history of metal deposition is more complex than in other clusters.

4 CAVITY SCENARIO

4.1 Surface brightness comparison

Here, we investigate the cavity origin scenario for the Perseus bay. We simulated an image of Perseus in which we took the surface

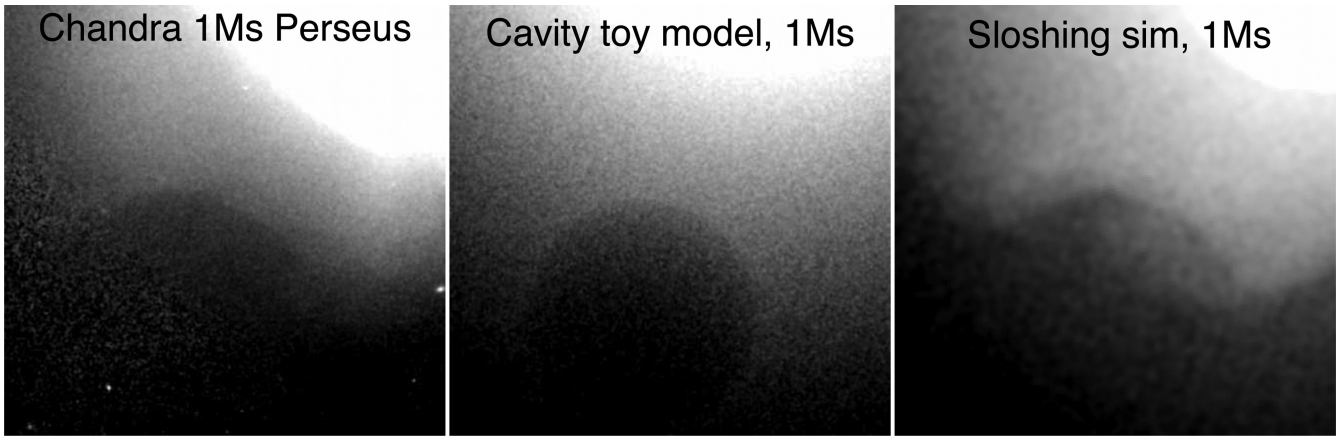

Figure 5. Comparing the image of the bay in Perseus (left) with a simulation of an empty spherical cavity in the same location and with the same size (centre), and the KH roll from the sloshing simulation of ZuHone & Kowalik (2016, right). The surface brightness profiles across these three cases are compared in the bottom panel of Fig. 2, where the cavity toy model is shown to overestimate the drop in surface brightness across the bay edge, with the discrepancy becoming even worse when an ellipsoidal cavity model is used.

brightness profile from the region of the cluster on either side of the bay and extrapolated this outwards. This acts to 'recreate' the original undisturbed ICM surface brightness profile before the formation of the bay. This surface brightness profile was then deprojected.

We then created a 3D cluster toy model, in which each element is weighted by the X-ray emissivity given by the deprojected surface brightness profile. In the simulation, a spherical cavity matching the dimensions and location of the bay was created by setting the X-ray emissivity of the elements within a suitably sized sphere equal to zero. The X-ray emissivity of the 3D toy model was then integrated along the line of sight to produce the 2D projected X-ray emissivity image. Using the *Chandra* response files and the *Chandra* PSF, we then produced a simulated *Chandra* image for an exposure time matching the real observation, to which an appropriate background was added.

The resulting simulated image from the toy model is shown in the central panel of Fig. 5. In the bottom panel of Fig. 2, we compare the projected surface brightness profiles across the real bay (black), and the cavity toy model (green dashed line). We see that the surface brightness drop expected for a spherically symmetric cavity is far more severe than we see in Perseus. We repeated this exercise using an ellipsoidal cavity instead, again matching the radius of curvature of the bay, and with the line-of-sight depth of the ellipsoid set equal to the width observed in the plane of the sky (60 kpc). Increasing the ellipticity of the removed cavity actually further increases the magnitude of the surface brightness drop, increasing the tension with observations. To match the observed drop in surface brightness, we find that the line-of-sight depth of the cavity would have to be around half its observed width on the sky, so that it is shaped like a rugby ball with the long side being viewed face on. This type of unusual geometry is in tension with the idea of rising spherical cap bubbles seen closer in the core of Perseus (Fabian et al. 2003). The inner bubbles at around 30–50 kpc from the cluster core already have a distinct spherical cap appearance, which should continue to develop as they rise outwards, so cavities at the radial distance of the bay (100 kpc) would be expected to have this form of geometry.

We repeat this exercise with the toy model, but this time for Abell 1795 and Centaurus. When the surface brightness profile across the toy model cavity rim is compared to the observed profile in the bottom panels of Fig. 3, we again find that the cavity toy model overestimates the decrement in X-ray surface brightness in both cases.

4.2 Temperature profile comparison

Here, we investigate the expected temperature profile across the inner rim of a cavity. To achieve this, we use both the deprojected temperature and density profiles on either side of the bay in our 3D cluster toy model, again 'recreating' the original undisturbed ICM. We then removed all of the emission from a spherical region matching the curvature of the bay, and produced projected spectra across the inner rim, with each temperature component correctly weighted by the emission measures along the line of sight.

For Perseus and Abell 1795, the resultant temperature profiles over the inner rim of the cavity toy model are shown in Figs 2 and 3 as the dashed green lines. In both cases, the temperature profile increase is very small, an increase of around 0.15 keV, which is much smaller than the observed increase of 0.8 keV for Perseus and 1–1.5 keV for Abell 1795. For Centaurus, because the bay is so close to the cluster centre, it is not possible to accurately use the toy model to reproduce the undisturbed ICM temperature distribution.

Making the line-of-sight depth of the cavity toy model smaller, in an attempt to match the surface brightness profile, acts to make the temperature jump across the inner rim even smaller (since less gas is removed), making the discrepancy with the observed temperature profile even worse. We find that for Perseus and Abell 1795, it is not possible to produce a cavity model that matches both the surface brightness jump and the temperature jump simultaneously.

4.3 Comparing with the jet power–metal radius relation

As a further test of the AGN-inflated cavity scenario, we consider the observed relationship between the AGN jet power ($P_{\rm jet}$) and the maximum radius at which an enhancement in metal abundance is seen (the Fe radius, $R_{\rm Fe}$). Kirkpatrick et al. (2011) have found a simple power-law relationship between these based on observations of clusters with AGN-inflated cavities, which is $R_{\rm Fe} = 58 \times P_{\rm jet}^{0.42}$ (kpc), where $P_{\rm jet}$ is in units of 10^{44} erg s^{-1}.

The jet power is estimated from the volume of cavity, V, and the pressure of the ICM, P, by dividing the total energy needed to grow the cavity, $4\,PV$ (which is the sum of the internal energy of the cavity and the work done in expanding it against the surrounding ICM), by a characteristic time-scale over which the cavity has risen, which is typically taken to be the sound crossing time from the cluster core to the centre of the cavity, $t_{\rm cs}$. Using our best-fitting ellipsoidal

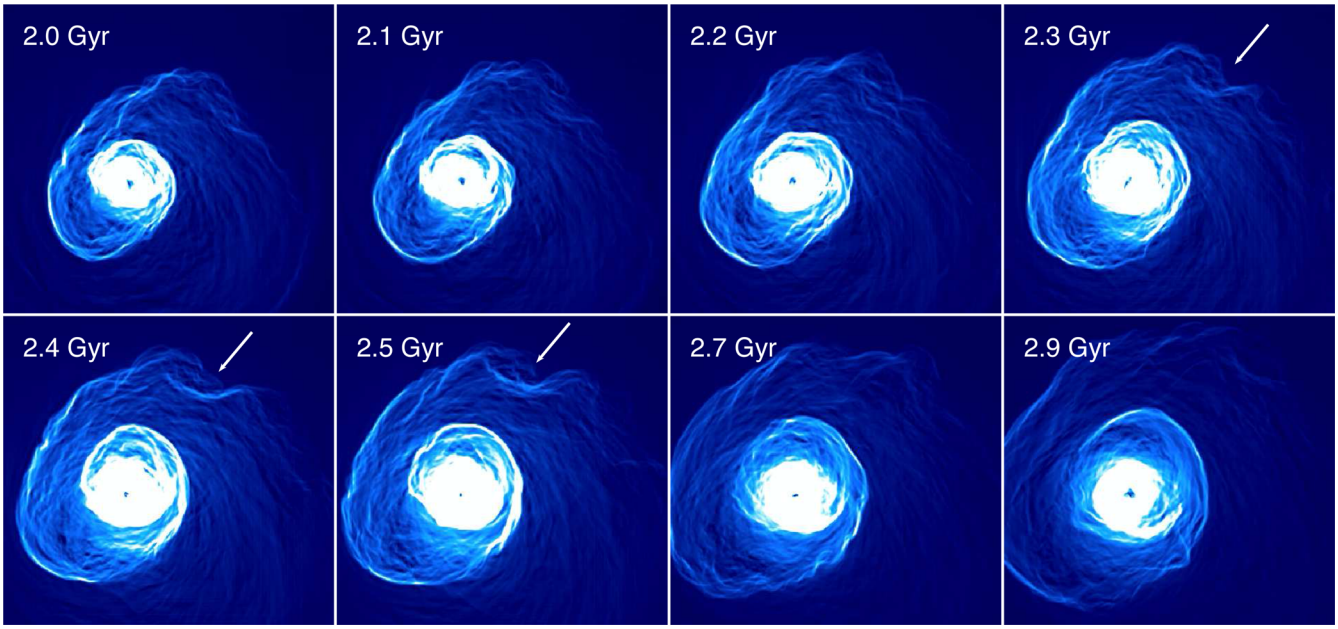

Figure 6. The evolution of KH roll structure in the simulations of ZuHone & Kowalik (2016) for $\beta = p_{\rm th}/p_{\rm B} = 200$, where the time shown is that which has elapsed since the moment of closest approach between the merging clusters. The simulated projected X-ray emissivity images have been filtered using GGM filtering to emphasize surface brightness edges. We see that KH rolls with similar structure to the sharp bay seen in Perseus can form (at 2.3 Gyr) and be destroyed (by 2.7 Gyr) on relatively short time-scales of ∼0.4 Gyr.

model for Perseus (which provides a lower bound to the jet power and the metal radius, for if the cavity were a sphere its volume and thus the jet power would be larger), we find a jet power of 1.2×10^{45} erg s^{-1}, which gives a metal radius of 165 kpc, much larger than the observed radius of the metal drop of 92 kpc from the cluster core.

Following the same procedure for Abell 1795, we find a jet power of 5×10^{44} erg s^{-1}, which gives a metal radius of 114 kpc, again much larger than the observed radius of the metal drop of 30 kpc from the cluster core. We extended the metallicity profiles outwards for both Perseus and Abell 1795, comparing to the azimuthal average, and found no evidence for an enhancement in metal abundance anywhere outside the bay edges. This lack of a metal abundance excess, and the strong disagreement with the Kirkpatrick et al. (2011) relation between jet power and metal radius, provides further evidence against the bays being the inner rims of AGN-inflated cavities.

5 SLOSHING SIMULATIONS

To search for concave cold fronts similar to the bay structure in Perseus, we explored the gas sloshing simulations made publicly available by ZuHone & Kowalik (2016) in their Galaxy Cluster Merger Catlog.[1] Of particular interest is the simulation 'Sloshing of the magnetized cool gas in the cores of galaxy clusters' taken from ZuHone et al. (2011), but with higher spatial resolution and an improved treatment of gravity (see Roediger & Zuhone 2012). In this FLASH AMR simulation, sloshing is initiated in a massive cool core cluster ($M_{200} = 10^{15}$ M$_\odot$) similar to Perseus. The simulations are projected along the axis perpendicular to the sloshing direction (i.e. along the z-axis, with sloshing occurring in the x–y plane). We stress that in Perseus, Abell 1795 and Centaurus, we are unlikely to be viewing the sloshing along such a perfectly perpendicular line of sight, so we expect there to be some line-of-sight projection effects in the real observations.

As shown in Fig. 6, when the outer cold front rises to around 150 kpc from the core, (similar to the position of the western cold front in Perseus), KH rolls form (shown by the white arrow), which remain stable over periods of 200–400 Myr, and which have the same X-ray morphology as the Perseus bay. In these simulations, an initially uniform ratio of the thermal pressure ($p_{\rm th}$) to magnetic pressure ($p_{\rm B}$), $\beta = p_{\rm th}/p_{\rm B}$, is assumed. As the sloshing progresses, the magnetic field becomes amplified along the cold fronts, restricting transport processes and inhibiting the growth of instabilities. These simulations have been run for different values of the initial β ratio, using the observed range of magnetic field strength from Faraday rotation and synchrotron radiation measurements (1–10 μG) as a guide. Simulation runs with $\beta = 1000$, 500, 200 and 100 are available. We find the best match to the Perseus observations is the $\beta = 200$ simulation, which is shown in Figs 6 and 7.

In the top two panels of Fig. 7, we compare the *Chandra* image of Perseus to the $\beta = 200$ sloshing simulation (which we have rotated) at a stage where the cold fronts are in the same relative location. There is a striking similarity between the location and size of the bay relative to the cold front in Perseus and the concave KH roll in the simulation. In both cases, the outer cold front on the right-hand side is around 150 kpc from the core, and the bay-shaped KH roll forms to the bottom left, around 135 deg clockwise from the furthest part of the cold front. In this proposed scenario, the AGN feedback has destroyed the inner cold front spiral (see the gradient filtered image in the bottom left of Fig. 7), but the outer cold front with the bay is sufficiently far from the core (∼150 kpc) that it remains intact.

Using the projected temperature simulation image (bottom right of Fig. 7), we compare the simulated temperature profile across the bay with the observed one in the top panel of Fig. 2, scaling by a small constant factor to account for the difference

[1] http://gcmc.hub.yt/

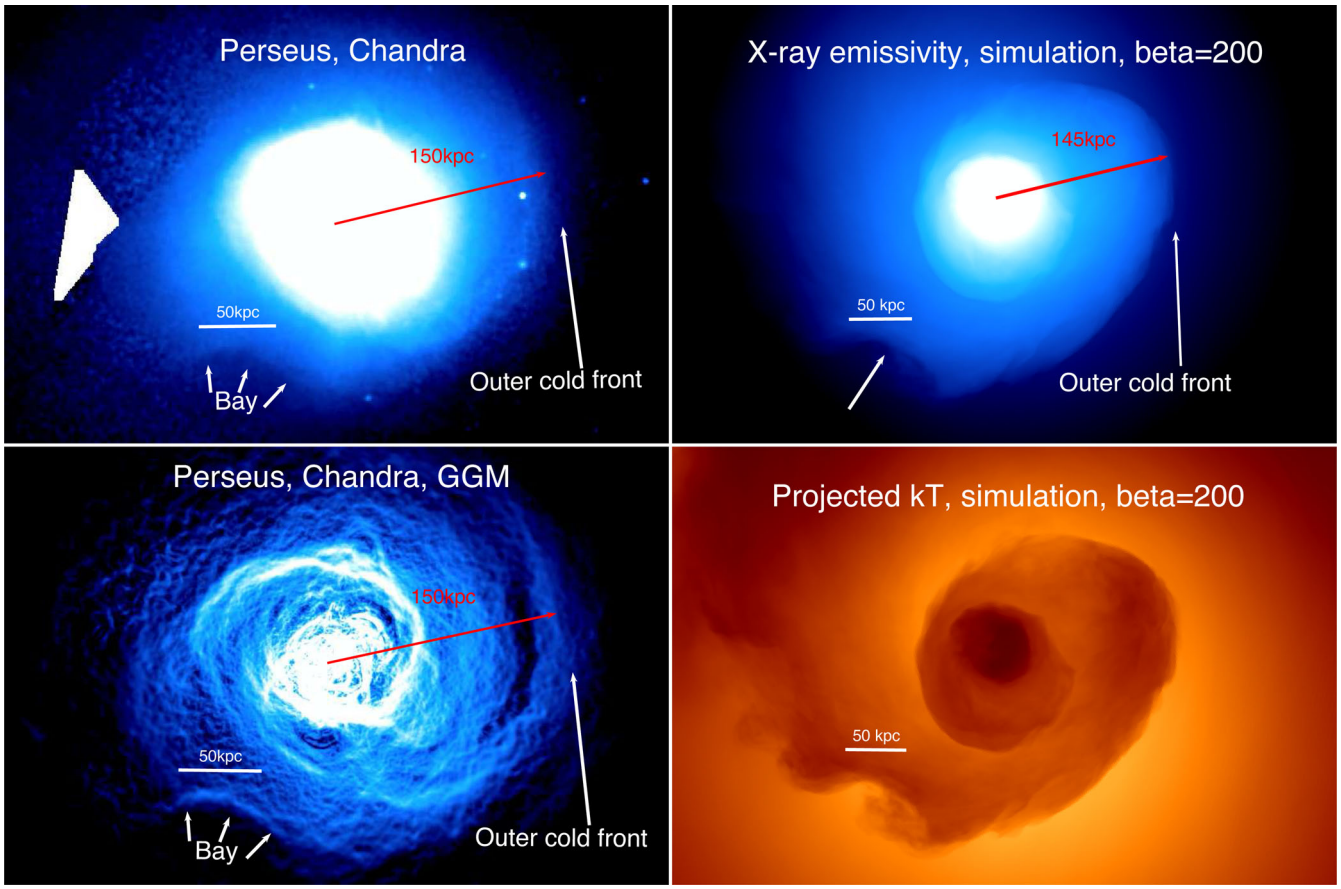

Figure 7. Comparing the outer cold front structure in Perseus with a minor merger simulation from ZuHone & Kowalik (2016, 'Sloshing of the magnetized cool gas in the cores of galaxy clusters', $\beta = 200$), 2.5 Gyr from the moment of closest approach of the merging clusters. The KH rolls develop into bay-like structures similar to that in the Perseus observation for a 0.4-Gyr period at this stage. The temperature drop structure over the KH roll resembles that in Perseus. The brevity of the period in which these structures are visible (0.4 Gyr) before being eroded away may explain why they are rare. The location of the bay relative to the western outer cold front is very similar to the location of the KH roll relative to the outer cold front in the sloshing spiral. The ratio of the sizes of these features is also very similar between simulation and observation.

in mass between Perseus (7×10^{14} $M_{\odot}$; Simionescu et al. 2011) and the simulated cluster (10^{15} $M_{\odot}$). We see that there is good agreement between the magnitude and shape of the temperature jump. We then compare the shape surface brightness profile across the bay edge, shown in the bottom panel of Fig. 2 as the dashed blue line. We see that the surface brightness profile is very similar to the observed profile and differs significantly from the cavity scenario (green dashed). The simulations assume a uniform metallicity of 0.3 $Z_{\odot}$, so we are unable to compare the observed metallicity profile jump to a simulated one.

In Fig. 8, we compare the observed cold front morphology of Perseus with the same time slice of the simulations, but this time for different values of β. We see that for higher values of β (1000 and 500), the amount of KH roll structure is far greater and inconsistent with the observations. For lower values of β (100), the formation of KH rolls is heavily suppressed and no significant bay-like features form.

If the bay in Perseus is a KH roll, then this provides the possibility of placing constraints on the thermal pressure to magnetic pressure ratio by comparing the observed images with the simulated images. The simulated KH rolls have a large spatial extent and distinct shape, making them far easier to see than the subtle structure behind the sharpest part of the cold front. Comparing KH roll structure between observations and simulations may therefore provide a straightforward way of constraining β.

The similar angle between the bay and main cold front in Abell 1795, shown in Fig. 4, suggests that a similar origin may be possible in A1795. However, the spatial scale of the features is roughly half that of the Perseus cluster. It is possible that the reason for this difference is simply that we are seeing Perseus and A1795 at different times from the merger that caused the sloshing.

Because the bay in Centaurus is much closer to the core, it is harder to attribute this to sloshing. However, searching through the simulations, we find a similar morphology of bay and cold front locations in the $t = 1.5$ Gyr time frame of the $\beta = 200$ simulation since the moment of closest approach of the merging clusters, shown in the central panel of Fig. 9. This bay is also not present in the same time frame of the higher magnetic field, $\beta = 100$ run of the simulations, again showing how sensitive such features are to the magnetic pressure level. We stress, however, that the spatial scale of the bay in these simulations is around a factor of 4 larger than the bay seen in Centaurus and that these simulations are for a much more massive cluster (10^{15} $M_{\odot}$) than the Centaurus cluster (2×10^{14} $M_{\odot}$; Walker et al. 2013), so the similarity is purely qualitative in this case. We note that the simulation images show linear features running parallel to and behind the outer main cold front, similar to the linear

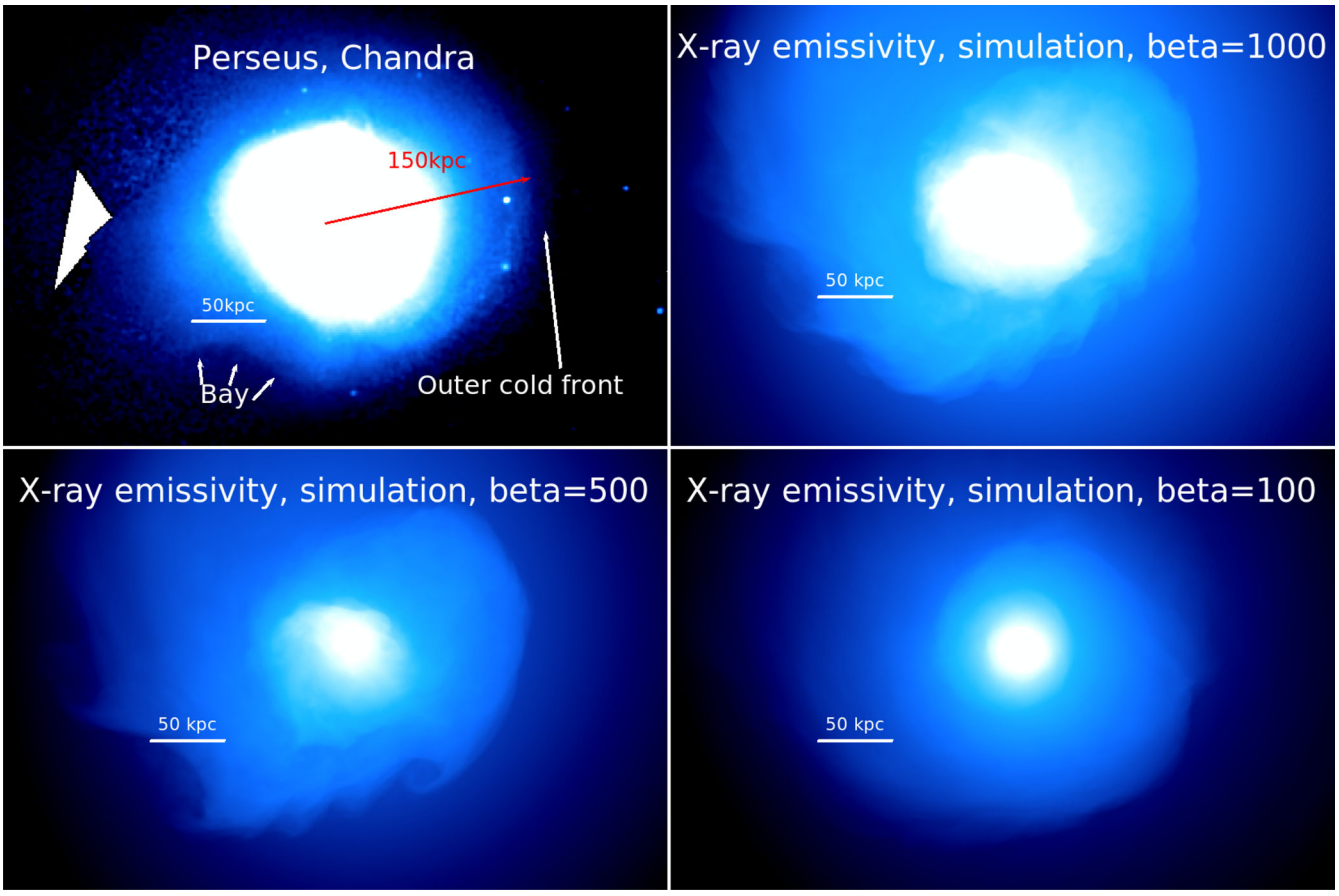

Figure 8. Comparing the *Chandra* observation of Perseus with simulations of KH rolls with different values of β (thermal pressure over magnetic pressure) for the same time slice as the simulation shown in Fig. 7. When β is high (1000 and 500), there is much more KH roll structure and the overall morphology disagrees with the observation. When β is low (100), the magnetic field is strong enough to prevent the formation of large bay-shaped KH rolls.

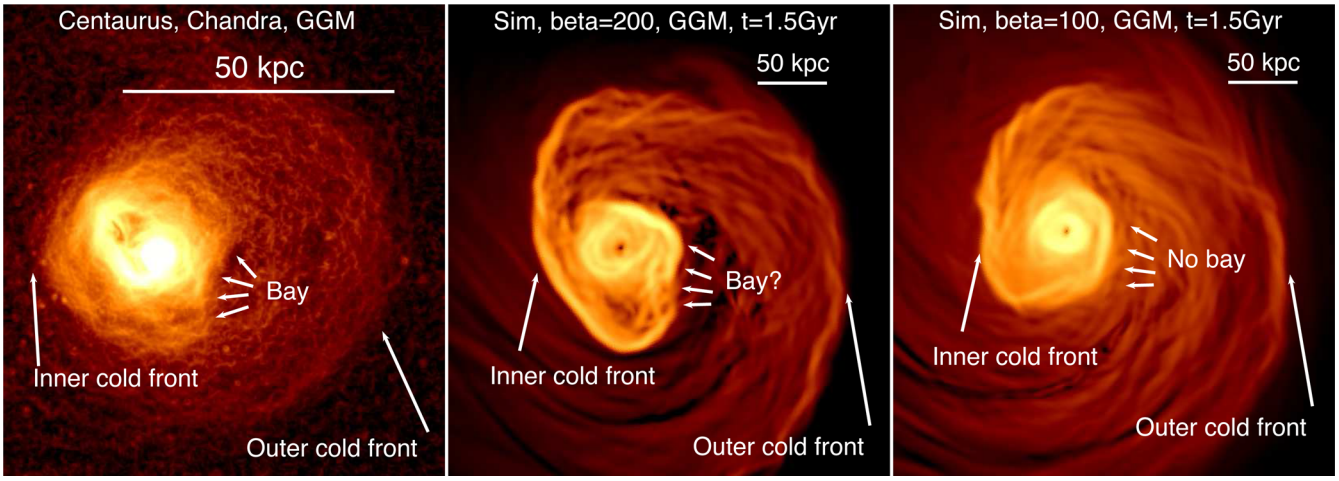

Figure 9. Comparing the bay and cold front morphology in Centaurus (left-hand panel) with simulations at 1.5 Gyr from the moment of closest approach of the merging clusters. We find a similar central bay in the $\beta = 200$ X-ray emissivity simulation (middle panel), which is not present in the $\beta = 100$ version of the same simulation with a stronger magnetic field (right-hand panel). We note, however, that the spatial scale on which this bay forms is much larger in the simulations than in Centaurus. All of these images have been processed with the GGM filter to emphasize gradient structure.

features found in the *Chandra* data in Sanders et al. (2016b, their fig. 7). As discussed in Werner et al. (2016), who found similar features in the Virgo cluster cold front, in the simulations these linear features are brought about by alternating areas of weak and strong magnetic pressure.

6 CONCLUSIONS

We have investigated the origin of concave 'bay'-shaped structures in three nearby clusters with deep *Chandra* observations (Perseus, Centaurus and Abell 1795), which have in the past been interpreted

as the inner rims of cavities inflated by AGN feedback. All three bays show temperature jumps coincident with the surface brightness jump, and have widths of the order of the Coulomb mean free path, making them consistent with cold fronts, but for the fact that they are concave instead of a convex.

We find that the observed temperature, density, metal abundance and radio distributions around the bays are incompatible with a cavity origin. By comparing with simulations of gas sloshing from ZuHone & Kowalik (2016), we find that the observed properties of the bays are consistent with large KH rolls, which produce similar concave cold front structures.

To test whether these bays could be cold fronts, we explored simulations of gas sloshing in a massive cluster from ZuHone & Kowalik (2016) to search for similar features. We find that, when the sloshing has developed to the point seen in Perseus, with an outer cold front at around 150 kpc from the core, large bay-shaped KH rolls resulting from KHIs can form. The relative size and location of these KH rolls to the cold front structure bear a striking similarity to the position of the bay in Perseus. The profiles of temperature and surface brightness are also in good agreement with the observed profile across the Perseus bay. We also find that the central bay in the Centaurus cluster, which lies much closer to the cluster core (around 15 kpc) than those in Perseus and A1795, can qualitatively be explained by gas sloshing rather than AGN feedback.

The shape of these instabilities is sensitive to the ratio of the thermal pressure to magnetic pressure, $\beta = p_{\rm th}/p_{\rm B}$. We find the best match to simulations with $\beta = 200$. When β is higher than this (1000 and 500) the level of instabilities is too great compared to observations, while for the $\beta = 100$ simulations the magnetic field strength is strong enough to prevent the formation of the instabilities. Due to the size of the KH rolls, they are far easier to see than the subtle differences in width of the cold fronts at their sharpest points. If the bay in Perseus is a KH roll, then this may provide a straightforward way of constraining β by comparing the observed image with simulated X-ray images. In particular, it potentially provides a simple way of ruling out simulations where the magnetic field is too high, as these prevent the formation of KH rolls, an effect that is far easier to see than subtle changes in the width of the traditional main convex cold front.

Whilst it is possible to put order of magnitude constraints on the magnetic field, more precise constraints using this method are likely challenging due to the sensitivity of KHIs to a number of factors. The initial perturbations used in the simulations are a factor in that stronger initial perturbations may lead to more pronounced KH rolls. The clarity of KH rolls at late stages of the simulations is also dependent on the spectrum of the initial perturbations.

One potential advantage of constraining the initial magnetic field using cold front structure is that we are probing the average magnetic field throughout the whole volume of the cluster, since the cold fronts rise from the core outwards and sample large volumes of the ICM. Measurements of the magnetic field in clusters using the Faraday rotation measure are typically limited to small sight lines probing small sections of the cluster ICM (see Taylor et al. 2006), and so can vary considerably by an order of magnitude (typically 1–10 μG) due to fluctuations in the magnetic field on scales of 5–10 kpc (Carilli & Taylor 2002). Comparing the observations with sloshing simulations therefore provide unique, large-scale average constraints on the overall magnetic field throughout the cluster volume.

In this paper, we have focused on three nearby clusters that have deep *Chandra* and radio data. A more systematic future study will be required, combining X-ray and radio data, to determine how common the 'bay' features are in the cluster population as a whole. Due to the complex spiral structure of gas sloshing, projection effects are more severe than for a situation consisting of AGN-inflated cavities in an otherwise undisturbed ICM. The best candidates for finding bays in other sloshing cluster cores are systems where we are viewing along a line of sight that is close to perpendicular to the plane of the sloshing.

The simulations we have looked at only vary the cluster magnetic pressure level whilst keeping the viscosity constant. The ICM viscosity also significantly affects the development of KHI rolls (Roediger et al. 2013), with a greater viscosity inhibiting the formation of instabilities. Future work is necessary to understand the relative contributions of these two factors to the overall cold front structure (Zuhone & Roediger 2016).

ACKNOWLEDGEMENTS

We thank the referee, E. Roediger, for helpful suggestions that improved the paper. SAW was supported by an appointment to the NASA Postdoctoral Program at the Goddard Space Flight Center, administered by the Universities Space Research Association through a contract with NASA. JHL is supported by NSERC through the discovery grant and Canada Research Chairs Program, as well as FRQNT. ACF acknowledges support from ERC Advanced Grant FEEDBACK. We thank John ZuHone for making the simulations shown in this paper publicly available. This work is based on observations obtained with the *Chandra* observatory, a NASA mission.

REFERENCES

Bautz M. W., Miller E. D., Sanders J. S., Arnaud K. A., Mushotzky R. F., Porter F. S., 2009, PASJ, 61, 1117
Carilli C. L., Taylor G. B., 2002, ARA&A, 40, 319
Ehlert S., McDonald M., David L. P., Miller E. D., Bautz M. W., 2015, ApJ, 799, 174
Fabian A. C., 2012, ARA&A, 50, 455
Fabian A. C. et al., 2000, MNRAS, 318, L65
Fabian A. C., Sanders J. S., Crawford C. S., Conselice C. J., Gallagher J. S., Wyse R. F. G., 2003, MNRAS, 344, L48
Fabian A. C., Sanders J. S., Taylor G. B., Allen S. W., 2005, MNRAS, 360, L20
Fabian A. C., Sanders J. S., Taylor G. B., Allen S. W., Crawford C. S., Johnstone R. M., Iwasawa K., 2006, MNRAS, 366, 417
Fabian A. C., Sanders J. S., Allen S. W., Canning R. E. A., Churazov E., Crawford C. S., 2011, MNRAS, 418, 2154
Gendron-Marsolais M. et al., 2017, MNRAS, preprint (arXiv:1701.03791)
Giacintucci S., Markevitch M., Venturi T., Clarke T. E., Cassano R., Mazzotta P., 2014, ApJ, 781, 9
Gitti M., Brunetti G., Setti G., 2002, A&A, 386, 456
Gitti M., Brunetti G., Feretti L., Setti G., 2004, A&A, 417, 1
Intema H. T., 2014, Astrophysics Source Code Library, record ascl:1408.006
Intema H. T., Jagannathan P., Mooley K. P., Frail D. A., 2017, A&A, 598, A78
Keshet U., 2010, preprint (arXiv:1011.0729)
Keshet U., Loeb A., 2010, ApJ, 722, 737
Kirkpatrick C. C., McNamara B. R., Cavagnolo K. W., 2011, ApJ, 731, L23
McNamara B. R. et al., 2000, ApJ, 534, L135
Markevitch M., Vikhlinin A., 2007, Phys. Rep., 443, 1
Markevitch M., Ponman T. J., Nulsen P. E. J., Bautz M. W., 2000, ApJ, 541, 542
Markevitch M., Vikhlinin A., Mazzotta P., 2001, ApJ, 562, L153
Mazzotta P., Giacintucci S., 2008, ApJ, 675, L9
Mohan N., Rafferty D., 2015, Astrophysics Source Code Library, record ascl:1502.007
Pfrommer C., Enßlin T. A., 2004, A&A, 413, 17
Roediger E., Zuhone J. A., 2012, MNRAS, 419, 1338
Roediger E., Brüggen M., Simionescu A., Böhringer H., Churazov E., Forman W. R., 2011, MNRAS, 413, 2057

Roediger E., Lovisari L., Dupke R., Ghizzardi S., Brüggen M., Kraft R. P., Machacek M. E., 2012, MNRAS, 420, 3632
Roediger E., Kraft R. P., Forman W. R., Nulsen P. E. J., Churazov E., 2013, ApJ, 764, 60
Sanders J. S., Fabian A. C., Russell H. R., Walker S. A., Blundell K. M., 2016a, MNRAS, 460, 1898
Sanders J. S. et al., 2016b, MNRAS, 457, 82
Sijbring L. G., 1993, PhD Thesis, Univ. Groningen
Simionescu A. et al., 2011, Science, 331, 1576
Swarup G., 1991, in Cornwell T. J., Perley R. A., eds, ASP Conf. Ser. Vol. 19, IAU Colloq. 131: Radio Interferometry. Theory, Techniques, and Applications. Astron. Soc. Pac., San Francisco, p. 376
Taylor G. B., Gugliucci N. E., Fabian A. C., Sanders J. S., Gentile G., Allen S. W., 2006, MNRAS, 368, 1500
Walker S. A., Fabian A. C., Sanders J. S., Simionescu A., Tawara Y., 2013, MNRAS, 432, 554
Walker S. A., Fabian A. C., Kosec P., 2014, MNRAS, 445, 3444
Walker S. A., Sanders J. S., Fabian A. C., 2015, MNRAS, 453, 3699
Walker S. A., Sanders J. S., Fabian A. C., 2016, MNRAS, 461, 684
Werner N. et al., 2016, MNRAS, 455, 846
ZuHone J. A., Kowalik K., 2016, ApJS, preprint (arXiv:1609.04121)
Zuhone J. A., Roediger E., 2016, J. Plasma Phys., 82, 535820301
ZuHone J. A., Markevitch M., Lee D., 2011, ApJ, 743, 16
ZuHone J. A., Markevitch M., Brunetti G., Giacintucci S., 2013, ApJ, 762, 78

APPENDIX A: OBSERVATIONS AND SPECTRAL EXTRACTION REGIONS

Table A1. *Chandra* data used in this paper.

Object	Obs ID	Exposure (ks)	RA	Dec.	Start Date
Perseus	3209	95.77	03 19 47.60	+41 30 37.00	2002-08-08
	4289	95.41	03 19 47.60	+41 30 37.00	2002-08-10
	4946	23.66	03 19 48.20	+41 30 42.20	2004-10-06
	4947	29.79	03 19 48.20	+41 30 42.20	2004-10-11
	6139	56.43	03 19 48.20	+41 30 42.20	2004-10-04
	6145	85.00	03 19 48.20	+41 30 42.20	2004-10-19
	4948	118.61	03 19 48.20	+41 30 42.20	2004-10-09
	4949	29.38	03 19 48.20	+41 30 42.20	2004-10-12
	6146	47.13	03 19 48.20	+41 30 42.20	2004-10-20
	4950	96.92	03 19 48.20	+41 30 42.20	2004-10-12
	4951	96.12	03 19 48.20	+41 30 42.20	2004-10-17
	4952	164.24	03 19 48.20	+41 30 42.20	2004-10-14
	4953	30.08	03 19 48.20	+41 30 42.20	2004-10-18
Centaurus	504	31.75	12 48 48.70	−41 18 44.00	2000-05-22
	4954	89.05	12 48 48.90	−41 18 44.40	2004-04-01
	4955	44.68	12 48 48.90	−41 18 44.40	2004-04-02
	5310	49.33	12 48 48.90	−41 18 44.40	2004-04-04
	16223	180.0	12 48 48.90	−41 18 43.80	2014-05-26
	16224	42.29	12 48 48.90	−41 18 43.80	2014-04-09
	16225	30.1	12 48 48.90	−41 18 43.80	2014-04-26
	16534	55.44	12 48 48.90	−41 18 43.80	2014-06-05
	16607	45.67	12 48 48.90	−41 18 43.80	2014-04-12
	16608	34.11	12 48 48.90	−41 18 43.80	2014-04-07
	16609	82.33	12 48 48.90	−41 18 43.80	2014-05-04
	16610	17.34	12 48 48.90	−41 18 43.80	2014-04-27
Abell 1795	See tables A1 and A2 from Walker et al. (2014)				

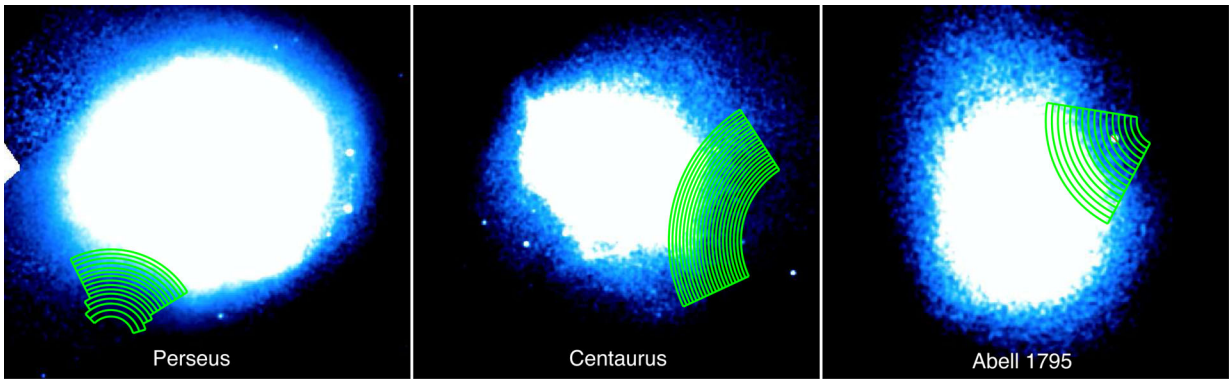

Figure A1. The regions used to extract the spectra for the profiles of temperature and metal abundance shown in Figs 2 and 3, overlaid on the *Chandra* observations.

This paper has been typeset from a TEX/LATEX file prepared by the author.